Article | Open Access

Energy Materials

Li *et al. Energy Mater.* **2026**, *6*, 600058 **DOI:**10.20517/energymater.2026.03

Axial electron-conduction engineering of single-atom copper catalyst for kinetic-fast oxygen reduction

Shuang Li#, Shiyu Li#, Jin Wang, Yanjie Wu, Jin Yan, Ke Liu, Yahui Yang*, Hui Su*

Keywords:
Axial coordination, single-atom, *in situ* synchronous radiation infrared spectroscopy, oxygen reduction reaction

Citation: Li, S.; Li, S.; Wang, J.; Wu, Y.; Yan, J.; Liu, K.; Yang, Y.; Su, H. Axial electron-conduction engineering of single-atom copper catalyst for kinetic-fast oxygen reduction. *Energy Mater.* **2026**, *6*, 600058. https://dx.doi.org/10.20517/energymater.2026.03

Received: 10 Jan 2026
First Decision: 18 Mar 2026
Revised: 14 Apr 2026
Accepted: 22 May 2026
Published: 9 Jun 2026

Academic Editor:
Ho Won Jang
Copy Editor:
Fangling Lan
Production Editor:
Fangling Lan

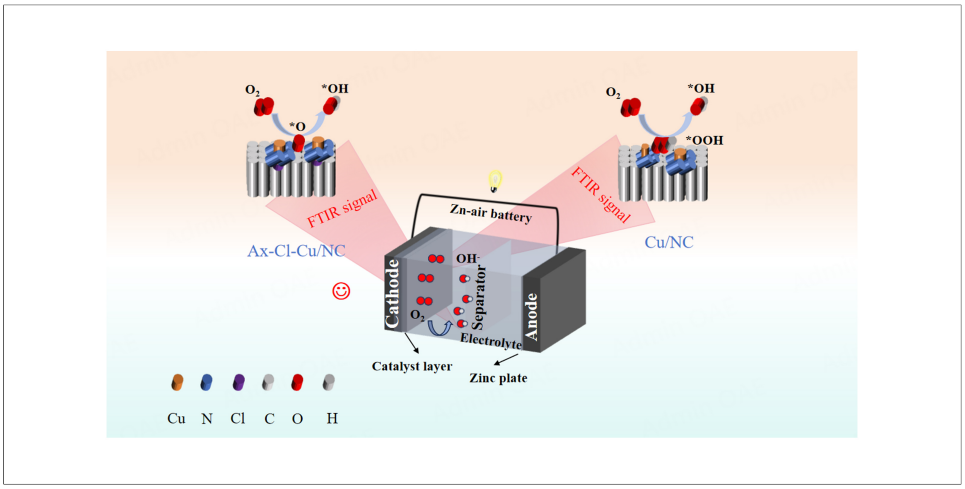

Abstract

Single-atom catalysts with metal-N_4 sites demonstrate good activity in the oxygen reduction reaction (ORR), yet the symmetric electronic structure limits its ability to differentially regulate oxygen-containing intermediates, resulting in sluggish kinetics. To address this, we have developed an axial chlorine-mediated strategy to break the symmetry of the copper-N_4 structure, thereby achieving superior ORR activity. Ax-Cl-Cu/NC catalyst was synthesized by coordinating an axial chlorine atom to the Cu-N_4 sites on an NC support. The as-prepared Ax-Cl-Cu/NC catalyst exhibits outstanding ORR performance, achieving nearly 99% four-electron selectivity and a large mass activity of 4,430.6 A g_{metal}^{-1} at 0.85 V - 67.4 times higher than Pt/C (65.73 A g_{metal}^{-1}). The superior performance of the Ax-Cl-Cu/NC catalyst is further demonstrated in a lab-assembled Zinc-air battery, which achieves stable operation for over 100 h. A series of experimental characterizations confirmed that the introduction of an axial chlorine atom reduced the electron density of the Cu center, alleviating the over-stabilization of oxygen intermediates and facilitated the cleavage of the O-O bond. This work establishes a new paradigm for

Key Laboratory of Chemical Biology and Traditional Chinese Medicine Research (Ministry of Education), Key Laboratory of Light Energy Conversion Materials of Hunan Province College, College of Chemistry and Chemical Engineering, Hunan Normal University, Changsha 410081, Hunan, China.
#Authors contributed equally.

***Correspondence to:** Prof. Yahui Yang, Prof. Hui Su, Key Laboratory of Chemical Biology and Traditional Chinese Medicine Research (Ministry of Education), Key Laboratory of Light Energy Conversion Materials of Hunan Province College, College of Chemistry and Chemical Engineering, Hunan Normal University, Changsha 410081, Hunan, China. E-mail: yangyahui2022@sina.com; suhui@hunnu.edu.cn

designing high-efficiency non-precious metal ORR catalysts.

INTRODUCTION

The oxygen reduction reaction (ORR) is the crucial cathodic process for advanced energy-conversion devices, such as zinc-air batteries (ZABs) and fuel cells[1-3]. However, its intrinsically sluggish kinetics, stemming from the four-electron-proton coupled transfer pathway, severely limits cathodic ORR performance[4]. The core of current alkaline ORR catalysts consists of precious metal (e.g., Pt) benchmarks, non-precious metal alternatives, and non-metallic carbon-based materials[5]. Among these, non-noble metal M-NC materials (M = Fe, Co, Mn, *etc.*), particularly single atom catalysts (SACs) featuring symmetrical planar M-N_4 coordination sites, have garnered significant interest due to their low cost, resource sustainability, and high atomic utilization efficiency[6]. Nevertheless, the inherent symmetric electronic configuration of M-N_4 catalysts restricts electron transfer, hindering the reaction kinetics[7-9]. To address this limitation, rationally modifying the local coordination environment (LCE) of M-N_4 catalysts—thereby disrupting their intrinsic symmetrical charge distribution—is critical for regulates the adsorption behavior of these intermediates. Consequently, the development of high-performance non-noble metal M-NC catalysts with tunable coordination geometries, high selectivity, and sufficient intrinsic activity has become a major research focus, yet remains a significant scientific and engineering challenge[10-13].

Numerous strategies including elemental doping, morphology engineering, and coordination control have been employed to improve the activity and stability of M-NC catalysts[14]. However, many current approaches primarily modify the in-plane local structure without fundamentally disrupting the symmetrical electron density distribution, creating a persistent bottleneck for performance enhancement[15]. Crucially, the activity and selectivity of SACs are intrinsically linked to the electron occupancy of the central metal's d-orbitals, as these orbitals directly participate in σ bonding with oxygen-containing intermediates[16]. Therefore, tailoring the microenvironment of the M-NC site presents an effective pathway to modulate *d*-orbital occupancy and, consequently, optimize the adsorption strength of key oxygen intermediates. To overcome this limitation, axial coordination engineering—introducing ligands above or below the M-N_4 plane with varying atomic radii and electronegativity—has emerged as a highly promising strategy[17-19]. For example, Yu and colleagues enhanced performance through heteronuclear metal synergistic effects, but this approach involves high costs associated with precious metals, while the ratio of diatomic species is difficult to control[20]. Gao and colleagues successfully constructed halogen-coordinated FeN_4X SACs on a nitrogen-doped carbon support via a halogen-assisted one-step pyrolysis strategy[21]. However, the complex multicomponent system makes the structure of the active sites ambiguous. Hu and colleagues successfully constructed atomically dispersed Sb site catalysts with an SbN_4-Cl structure for efficient ORR[22]. Nevertheless, the large ionic radius of the Sb metal center limits its coordination stability with nitrogen, and its cost is relatively high compared to Cu. Indeed, Cu with its high *d*-electron density, exhibits strong orbital hybridization with the *p* orbitals of oxygen molecules, precisely illustrating this interaction. Yet, when anchored within an NC matrix, Cu typically adopts a symmetric Cu-N_4 configuration[23]. This planar symmetry impedes the optimal adsorption/desorption of the *OOH intermediate, a critical step in the four-electron ($4e^-$) ORR pathway[24-26]. This approach of introducing axial Cl deliberately breaks the planar symmetry and conjugation, inducing electron redistribution within the Cu-N_4 center[13,27]. Herein, "breaks the planar symmetry and conjugation" refers to the distortion of the originally highly symmetric square-planar Cu-N_4 configuration caused by the introduction of an axial Cl ligand. This axial coordination disrupts the planar ligand field, leading to a non-centrosymmetric geometric structure and a reorganized electronic configuration of the Cu center. Such precise electronic structure modulation holds significant potential for enhancing the intrinsic activity and selectivity of Cu-based SACs towards the efficient $4e^-$ ORR[2,4,28-31].

Herein, to address the limitations of symmetric M-N_4 sites, we designed an axial chlorine-coordinated copper single-atom catalyst (denoted Ax-Cl-Cu/NC). X-ray photoelectron spectroscopy (XPS) and extended X-ray absorption fine structure (EXAFS) confirm that axial Cl coordination induces both electronic symmetry breaking and geometric symmetry breaking at the Cu center, while *in situ* infrared spectroscopy further reveals the dynamic evolution of *OOH/*O intermediates and the accelerated cleavage of the O-O bond. Consequently, Ax-Cl-Cu/NC exhibits significantly enhanced ORR activity and stability. The optimized catalyst achieves exceptional performance metrics: near-unity $4e^-$ selectivity (99%) and a high half-wave potential (0.89 V). When deployed as the cathode in a ZAB, Ax-Cl-Cu/NC delivers an impressive open-circuit voltage (OCV) of 1.53 V and a maximum power density (156.6 mW cm^{-2}) surpassing that of commercial Pt/C (127.3 mW cm^{-2}). Our work establishes a novel paradigm for M-NC catalyst design through concurrent "electronic structure-coordination geometry" regulation. This dual-dimensional modulation strategy opens new avenues for developing highly efficient ORR electrocatalysts.

EXPERIMENTAL

Materials

The copper source, copper(II) nitrate trihydrate ($Cu(NO_3)_2·3H_2O$, ≥ 99% purity), was purchased from Aladdin (China). The nitrogen/carbon sources, 2-methylimidazole and zinc nitrate hexahydrate ($Zn(NO_3)_2·6H_2O$, both ≥ 99% purity), were also purchased from Aladdin (China). Sodium chloride (NaCl, analytical grade) was used as the chlorine source and purchased from Sinopharm Chemical Reagent (China). Methanol (CH_3OH, ≥ 99.5%) and ethanol (C_2H_5OH, ≥ 99.7%), both of analytical grade, were purchased from Macklin (China), while deionized water was prepared in the laboratory. Nafion solution (5 wt%) was purchased from Sigma-Aldrich (USA), and commercial Pt/C (20 wt%) was purchased from Macklin (China). Potassium hydroxide (KOH, ≥ 99.99% purity) used as the electrolyte was purchased from Aladdin (China). All aqueous solutions were prepared using 18.2 MΩ·cm Millipore water purified in a Millipore system. All chemicals were of analytical grade and used without further purification.

Synthesis of ZIF-8

9.5 g of $Zn(NO_3)_2·6H_2O$ and 20 g of 2-methylimidazole were dissolved in 200 mL of methanol, respectively. The reaction mixture was then stirred at room temperature for 24 h. The precipitate was collected by centrifugation at 6,000 rpm for 6 min, and the resulting solid was washed three times with methanol, and dried in a vacuum oven at 70 °C for about 12 h.

Synthesis of NC

The ZIF-8 powder prepared above was ground and then high temperature pyrolysis. Under the protection of nitrogen (N_2) atmosphere, the temperature of the furnace was increased to 1,000 °C at a rate of 5 °C /min and maintained at a constant temperature for 2 h.

Synthesis of Cu/NC

0.8 g of ZIF-8 was homogeneously dispersed in 100 mL of methanol, followed by the slow dropwise addition of a methanolic solution of 1 mmol of $Cu(NO_3)_2·3H_2O$ to the above system, and magnetic stirring (500 rpm) for 6 h at room temperature (25 ± 1 °C). After centrifugation (8,000 rpm, 2 min), vacuum dried at 70 °C for 12 h. The resulting precursor was pyrolyzed in a nitrogen atmosphere at 5 °C/min up to 1,000 °C for 2 h.

Synthesis of Ax-Cl-Cu/NC

The Ax-Cl-Cu/NC catalyst was prepared by mechanical milling combined with high-temperature pyrolysis: Cu/NC was fully milled and mixed with NaCl at a mass ratio of 1:1, heated to 1,000 °C at an elevated rate of 5 °C /min under nitrogen atmosphere and held for 2 h. In addition, we prepared samples with different NaCl to Cu ratios (0.75:1 and 1.25:1) by grinding for comparison. The product was washed with distilled water

three times (30 mL each time) to completely remove the residual NaCl, followed by vacuum drying at 70 °C for 12 h.

The additional detailed experimental data, such as reagents, characterizations, and electrochemical measurements, are provided in the Supplementary Materials.

RESULTS AND DISCUSSION

Morphology and structure characterizations of Cu based catalysts

Ax-Cl-Cu/NC catalyst in which coordination-regulated Cu sites were confined in N-doped carbon carrier was prepared via a facile pyrolysis strategy. As seen in Figure 1A, ZIF-8 was prepared using a common method, and then the copper source (Cu precursor) and chlorine source (Cl precursor) were anchored to the ZIF-8 substrate surface using injection and grinding methods[7,32]. Use a microinjection to drop metallic copper into the ZIF-8 solution, allowing Cu to be uniformly and stably anchored on the substrate. Grind NaCl and Cu-ZIF in a 1:1 ratio so that the Cl source can coordinate with Cu along the axial direction. The final sample is named Ax-Cl-Cu/NC catalyst and Cu/NC samples without sodium chloride were used as controls. Analyze the morphology of the sample using scanning electron microscopy (SEM) and transmission electron microscopy (TEM). As shown in Supplementary Figure 1A and B, both Ax-Cl-Cu/NC and Cu/NC exhibit a rhombic dodecahedral morphology similar to that of ZIF-8. High-resolution TEM (HRTEM) analysis showed [Supplementary Figure 1C and D] that no discernible lattice fringes were observed in either the Ax-Cl-Cu/NC or Cu/NC samples. X-ray diffraction (XRD) patterns further corroborate this conclusion. Only two distinct carbon diffraction peaks appear in the diffraction patterns of all samples [Supplementary Figure 2A] and XRD test results of samples at different temperatures [Supplementary Figure 2B] indicate that the form of Cu presence is not significantly related to temperature. Raman spectroscopy was further employed to examine the carbon structure. As displayed in Supplementary Figure 2C, both catalysts exhibit similar I_D/I_G ratios (≈1.001), indicating negligible change in graphitization degree upon axial Cl introduction. The specific morphology of Cu was further investigated using high-angle annular dark-field STEM (HAADF-STEM) [Figure 1B and C]. The results show that only isolated speckled bright spots (marked by red circles) appear in the Cu/NC and Ax-Cl-Cu/NC samples, indicating that metallic copper is atomically dispersed on the NC material.

The energy-dispersive X-ray spectroscopy (EDS) elemental distribution map of Ax-Cl-Cu/NC [Figure 1D] shows that carbon (C), nitrogen (N), copper (Cu), and chlorine (Cl) elements are uniformly distributed in the nitrogen carbon co-doped matrix, indicating the successful introduction of Cl. Further analysis of the coordination environment of Cu was performed using EXAFS spectroscopy [Figure 1E]. Compared with Cu foil and CuO, the prominent peak at around ~1.5 Å can be attributed to the Cu-N bond, while no Cu-Cu scattering peak appears in Ax-Cl-Cu/NC and Cu/NC. Interestingly, the Cu-N peak in Ax-Cl-Cu/NC shifted positively by 0.06 Å compared to the Cu/NC sample, indicating the formation of a Cu-Cl coordination structure. In addition, the fitted curves of the k^3-weighted Cu *K*-edge EXAFS spectra in Figure 1E, as well as the corresponding data listed in Supplementary Table 1 for Ax-Cl-Cu/NC and Cu/NC, indicate that the coordination number (CN) of the Cu-N bond in Cu/NC is 3.9. For Ax-Cl-Cu/NC, the additional Cu-Cl pathway was taken into account during the fitting process, containing 3.9 Cu-N bonds and 1.0 Cu-Cl bonds. To highlight the local structure around the Cu site and the axial Cl coordination, a local structure model is shown in Figure 1E. These results demonstrate that the Cl element is indeed involved in the coordination of $Cu-N_4$ in an axial fashion. Quantitative analysis by inductively coupled plasma optical emission spectroscopy (ICP-OES) showed that the copper loading of Ax-Cl-Cu/NC and Cu/NC was 1.1 and 1.4 wt%, respectively.

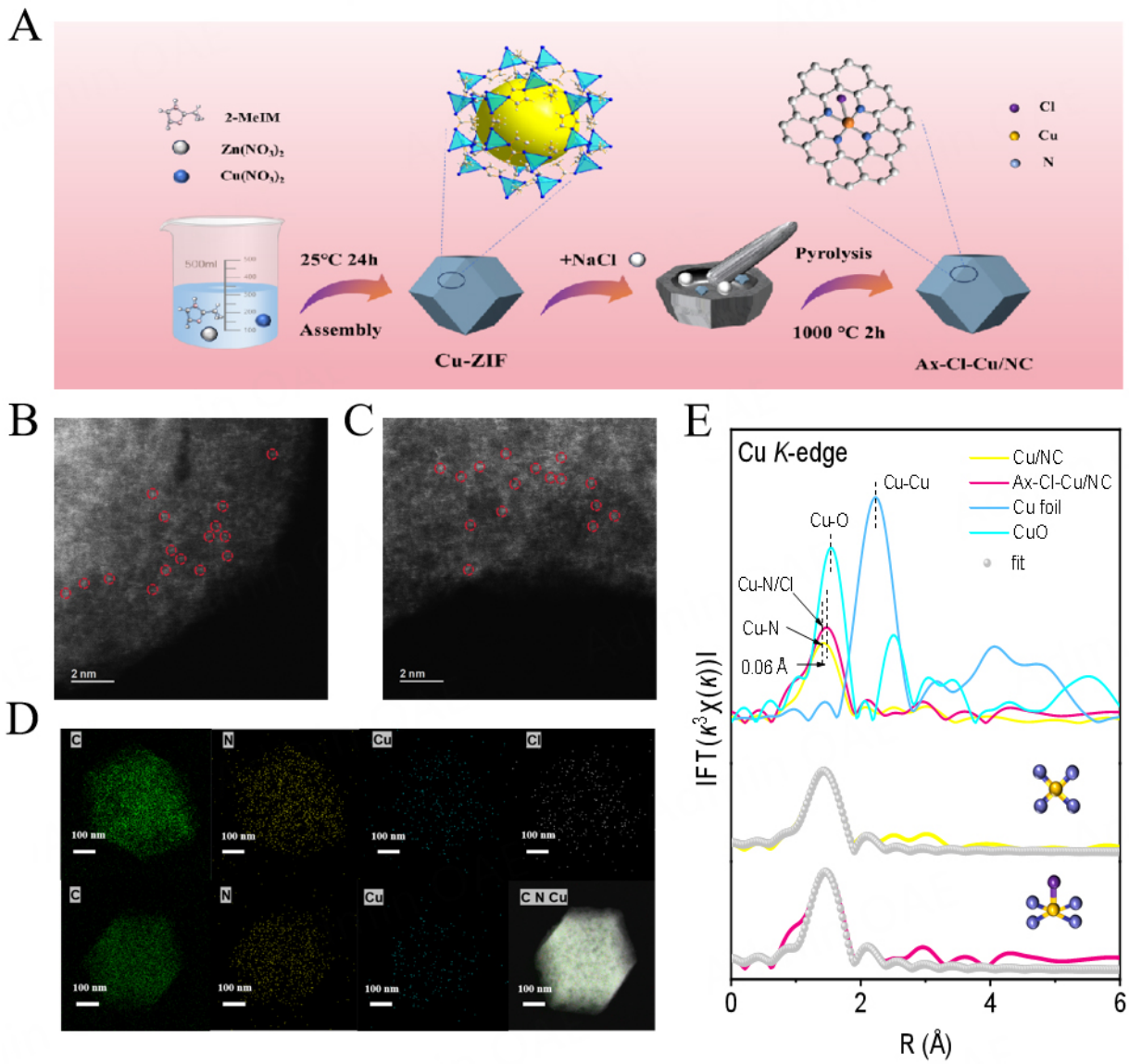

Figure 1. (A) Preparation process of Ax-Cl-Cu/NC, HAADF-STEM of (B) Cu/NC and (C) Ax-Cl-Cu/NC, (D) TEM-EDS mapping image of Cu/NC and Ax-Cl-Cu/NC (green, yellow, blue and white represent C, N, Cu and Cl elements), (E) FT-EXAFS spectra of the Cu *K*-edge for Ax-Cl-Cu/NC and Cu/NC and fitting spectra of Cu/NC. The inset shows Cl, Cu, and N atoms indicated by purple, gold and blue.

Analysis of electronic structure and LCE

The chemical composition and structure of each element in the catalyst were examined systematically. Firstly, the chemical composition of the catalyst was characterized using XPS. The full spectrum analysis in Supplementary Figure 3A shows the Cl characteristic peak, indicating the successful doping of Cl element in the Ax-Cl-Cu/NC catalyst. The C 1*s* XPS spectra of different samples are presented in Supplementary Figures 3B-D. All samples show a deconvoluted peak at 284.8 eV corresponding to C-N bonds, indicating that carbon and nitrogen are indispensable components of the catalysts. The local electronic states of each atom in the Ax-Cl-Cu/NC catalyst were further investigated by soft X-ray absorption near-edge structure spectroscopy (XANES) [Figure 2A], we can see that Cu/NC and Ax-Cl-Cu/NC have peaks at ~401 eV, which are attributed to Cu-N coordination. The regulatory effect of Cl atoms on Cu-N bonds was further revealed by XPS of N 1*s*, as shown in Figure 2B. It is worth noting that the binding energy of Cu-N bonds in Ax-Cl-Cu/NC shifted approximately 0.2 eV to the high energy compared to Cu/NC. Regarding the *L*-edge of Cl in the Ax-Cl-Cu/NC catalyst [Figure 2C], we can see two large peaks, G and H,

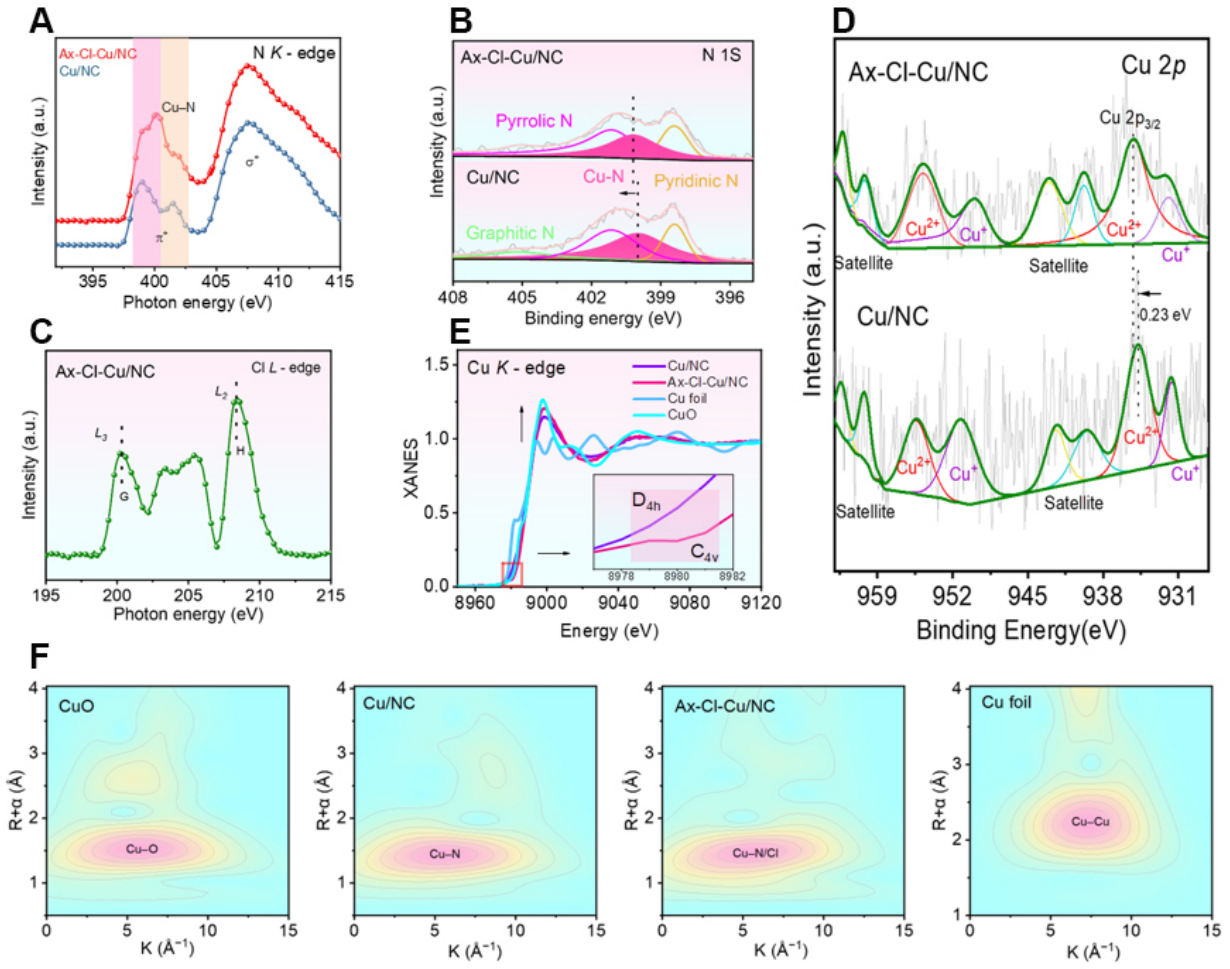

Figure 2. (A) N *K*-edge XANES spectra of Ax-Cl-Cu/NC and Cu/NC, (B) N 1s XPS spectra, (C) Cl *L*-edge XANES spectra of Ax-Cl-Cu/NC, (D) Cu 2*p* XPS spectra of Ax-Cl-Cu/NC and Cu/NC, (E) Cu *K*-edge XANES spectra and (F) Wavelet transforms of k^2-weighted XAFS spectra of CuO, Cu/NC, Ax-Cl-Cu/NC, Cu foil.

which correspond to Cl-metal peaks, proving that Cl interacts with metal Cu[33,34]. In the high-resolution Cl 2*p* spectrum of Ax-Cl-Cu/NC [Supplementary Figure 4], the Cu-Cl characteristic peak at 197.88 eV, directly confirming the presence of Cu-Cl bonds in the catalyst. The Cu 2*p* fine spectrum [Figure 2D] clearly shows that the peak of Cu^{2+} in Ax-Cl-Cu/NC shifts to a higher binding energy by 0.23 eV. This is because Cl has extremely high electronegativity and can attract electrons from around copper, leading to an increase in the valence state of Cu. Collectively, these findings suggest that the introduction of axial Cl induces a redistribution of *d*-band electrons around Cu, shifting electron density overall toward Cl, breaking the local electron symmetry around Cu, and thus potentially enhancing its ORR performance. The Cu *K*-edge XANES spectrum [Figure 2E] shows that the absorption energy of Ax-Cl-Cu/NC lies between that of Cu foil and CuO, close to that of +2 valent copper, and its absorption edge is slightly shifted to the high energy compared to Cu/NC, indicating that Cl coordination causes electron transfer from Cu to Cl, thereby increasing the apparent valence state of Cu. In the inset, the pre-edge peak Ax-Cl-Cu/NC shows a distinct small peak compared to Cu/NC, suggesting that the presence of Cl disrupts the symmetric configuration of CuN_4. Wavelet transform (WT)-EXAFS analysis further supports the above conclusion [Figure 2F]. The WT-EXAFS spectrum of Ax-Cl-Cu/NC shows slight differences compared to Cu/NC, indicating specific interactions between Cu and Cl atoms. Some fitting plots related to XAFS are provided in the supplementary information [Supplementary Figures 5 and 6]. The above X-ray absorption spectroscopy (XAS) results and XPS data form a complete chain of evidence, jointly confirming that Cl atoms the symmetry of electronic distribution through electron transfer and coordination effects.

Electrochemical oxygen reduction performance

Informed by the analysis of these results, the systematic evaluation of the ORR performance of the catalyst was carried out in an O_2-saturated 0.1 M KOH electrolyte using the RotatingRing-disk Electrode technique (DC DSR, PHYCHEMI)[35]. As shown in Figure 3A, Ax-Cl-Cu/NC exhibited optimal ORR activity with a half-wave potential ($E_{1/2}$) of 0.89 V, which was significantly better than 20 wt% Pt/C (0.86 V), Cu/NC (0.85 V), and NC (0.63 V). Meanwhile, the ORR performance achieved by Ax-Cl-Cu/NC is superior to those of most recently reported SACs [Supplementary Table 2]. The experimental results of pyrolysis temperature optimization in Supplementary Figure 7 showed that the sample prepared by pyrolysis at 1,000 °C had the highest half-wave potential, which fully verified the key role of high-temperature treatment on the formation of active sites. We also measured the linear scan voltammogram curves of different NaCl-to-Cu/NC mass ratios, and the results confirmed that the 1:1 ratio gave the best performance [Supplementary Figure 8]. The onset potential of Ax-Cl-Cu/NC was 0.977 V (corresponding to 5% diffusion-limited current), which was slightly higher than that of Pt/C (0.973 V), and its limiting current density reached 6.12 mA cm^{-2}, which was significantly higher than that of Pt/C (5.02 mA cm^{-2}, Supplementary Figure 9), which indicates that the catalyst has better mass transfer efficiency for O_2. All catalysts were tested under the same conditions [Supplementary Figure 10]. As shown in Figure 3B, the kinetic current density (J_K) of Ax-Cl-Cu/NC at 0.85 V is as high as 17.399 mA cm^{-2}, which is 3.71 times higher than that of Pt/C (4.693 mA cm^{-2}), which directly confirms that the strengthening effect of Cl coordination on the CuN_4 active site. As can be seen from Figure 3C, the Tafel slope of Ax-Cl-Cu/NC was 109.92 mV dec^{-1}, which was significantly lower than that of Pt/C (131.2 mV dec^{-1}), Cu/NC (207.73 mV dec^{-1}), and NC (215.11 mV dec^{-1}), which fully proved its faster reaction kinetics. Ax-Cl-Cu/NC showed a turnover frequency (TOF) of 734.8 h^{-1} at 0.85 V and a mass activity (MA) of 4,430.6 A g_{metal}^{-1}, which were 22.1 and 67.4 times higher than those of Pt/C (33.2 h^{-1}, 65.73 A g_{metal}^{-1}), respectively [Figure 3D]. This excellent performance is rooted in the induced effect of Cl atoms on Cu 3*d* energy-band electrons, which promotes the ORR kinetics. To understand the superior ORR activity of the Ax-Cl-Cu/NC catalyst, the electrochemical active surface areas (ECSA) of different catalysts were measured (ECSA = C_{dl}/C_s, where C_{dl} is the double-layer capacitance and Cs is the specific capacitance of graphitic carbon; here C_s was taken as 0.04 mF cm^{-2})[36]. Supplementary Figure 11A shows that among the catalysts prepared in this study, the Ax-Cl-Cu/NC catalyst exhibits the highest ECSA value (349 m^2 g^{-1}), outperforming Cu/NC (288 m^2 g^{-1}) and Pt/C (79 m^2 g^{-1}), confirming that this catalyst has the most active electron transfer centers during ORR. By normalizing the specific ORR activity with the ECSA values, the intrinsic activity of the Ax-Cl-Cu/NC catalyst was determined to be 0.0139 mA cm^{-2}, which is 3.18 times higher than that of the Cu/NC catalyst [Supplementary Figure 11B]. This indicates that the high intrinsic ORR activity of the Ax-Cl-Cu/NC catalyst originates from its unique Cl coordination environment. Electrochemical impedance spectroscopy (EIS) technique, and the results showed that Ax-Cl-Cu/NC has a lowest reaction resistance and thus exhibits a higher reactivity advantage [Supplementary Figure 12].

The electron transfer number (n) and H_2O_2 yield of the catalyst are key indicators of ORR selectivity[37]. As measured by the rotating ring disk electrode (RRDE) technique [Figure 3E], the electron transfer number of Ax-Cl-Cu/NC is about 3.96, which is close to the ideal $4e^-$ transfer pathway, confirming its excellent ORR selectivity. The results of fitting the Koutechy-Levich (K-L) equation at different rotational speeds [Supplementary Figures 13 and 14] showed a high degree of consistency in the linear slopes, which further verified that the catalyst followed an efficient $4e^-$ reaction mechanism over a wide range of mass transfer. The H_2O_2 yield of Ax-Cl-Cu/NC was only 2.03 %, which was significantly lower than that of the other reference samples, suggesting that Cl doping inhibits the occurrence of side reactions. More importantly, this outstanding activity can remain stable even under rigorous testing conditions. Additionally, the stability and durability of the Ax-Cl-Cu/NC catalyst were measured via chronoamperometry (CA) and accelerated durability testing (ADT). ADT results showed [Figure 3F] that the half-wave potential ($E_{1/2}$) of Ax-Cl-Cu/NC only decays ~7 mV after long-term cycling, exhibiting a structural stability superior to that of most SACs.

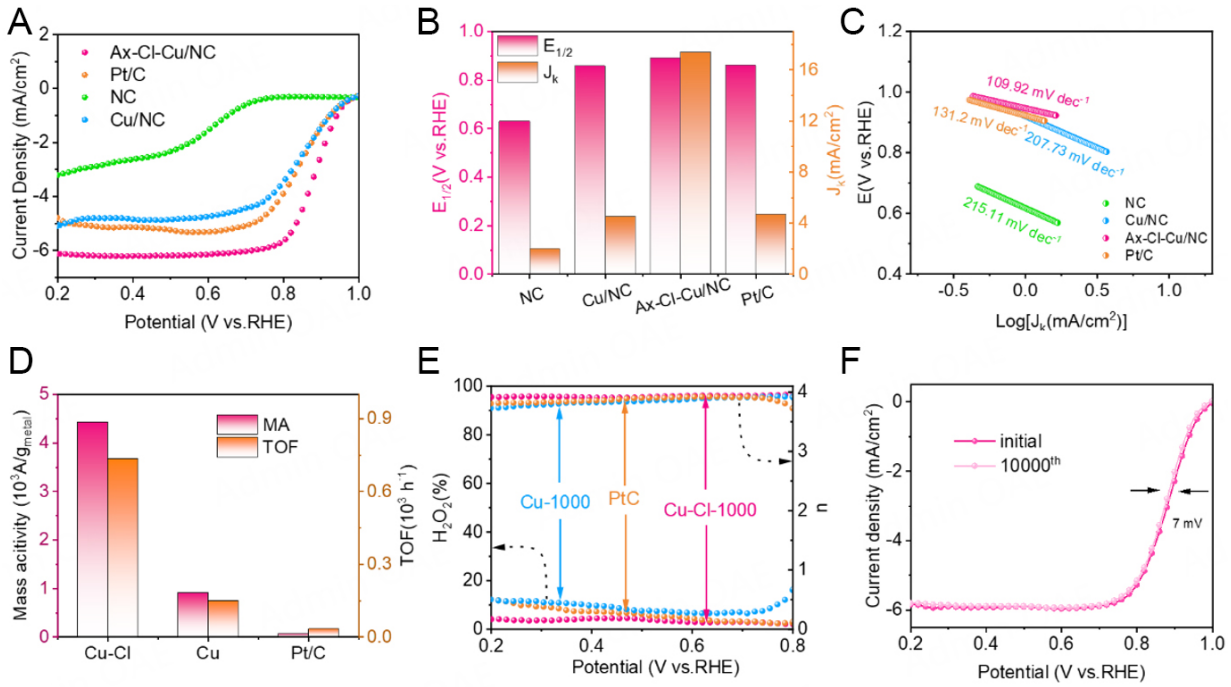

Figure 3. (A) Polarization curves at 1,600 rpm, (B) kinetic current density (J_k) at 0.85 V and $E_{1/2}$, (C) Tafel profile kinetics, (D) mass activity (MA) and turnover frequency (TOF), (E) electron transfer number and H_2O_2 yield of the Ax-Cl-Cu/NC and reference sample, (F) durability test plots (ADT) of Ax-Cl-Cu/NC in 0.1 M KOH solution.

However, the $E_{1/2}$ of Pt/C and Cu/NC catalysts decreased by 18 and 11 mV, respectively [Supplementary Figure 15]. The Ax-Cl-Cu/NC exhibits reliable stability with better methanol resistance and lower current density attenuation (< 5%) after 40 h of CA testing at 0.7 V [Supplementary Figures 16 and 17]. Interestingly, the XPS of Cl in Ax-Cl-Cu/NC after the reaction shows no significant change compared to before the reaction, indicating its excellent stability [Supplementary Figure 4]. Post-durability XPS analysis shows no significant change in the Cl 2p peak position or intensity compared to the fresh sample, with the Cl atomic percentage remaining nearly unchanged (from 0.90% to 0.85%). This confirms that the axial Cl species do not undergo noticeable leaching or changes in chemical state under alkaline conditions. The experimental evidence indicates that the axial Cl in the Ax-Cl-Cu/NC catalyst exhibits good structural stability during alkaline ORR operation. By combining various characterizations and performance test results, the introduction of chlorine achieved a simultaneous enhancement of ORR selectivity and stability.

In situ characterizations of the evolution of active sites

To elucidate the mechanism behind the outstanding ORR activity and stability of Ax-Cl-Cu/NC, *in-situ* EIS and *in-situ* synchronous radiation infrared spectroscopy (SRIR) technique studies were conducted. The distribution of relaxation times (DRT) of Cu/NC and Ax-Cl-Cu/NC at different voltages [Figure 4A and B] reveal two dominant characteristic peaks, corresponding to mass transport (10^{-1}~10^{0} Hz) and charge transport (~10^{1} Hz) processes, respectively[38-40]. Comparative analysis demonstrates that Ax-Cl-Cu/NC exhibits significantly reduced peak intensities with all peaks shifted toward higher frequencies compared to Cu/NC. Charge Transfer Resistance (R_{ct}) is related to the charge transfer at the electrode interface; the higher the R_{ct}, the weaker the charge transfer. Figure 4C shows that the reaction kinetics of Ax-Cl-Cu/NC are stronger than those of Cu/NC at any voltage. The EIS plots of the Ax-Cl-Cu/NC and Cu/NC catalysts at different voltages are shown in Supplementary Figure 18. These observations indicate that Ax-Cl-Cu/NC possesses lower charge transfer resistance, which are more favorable for facilitating the ORR process.

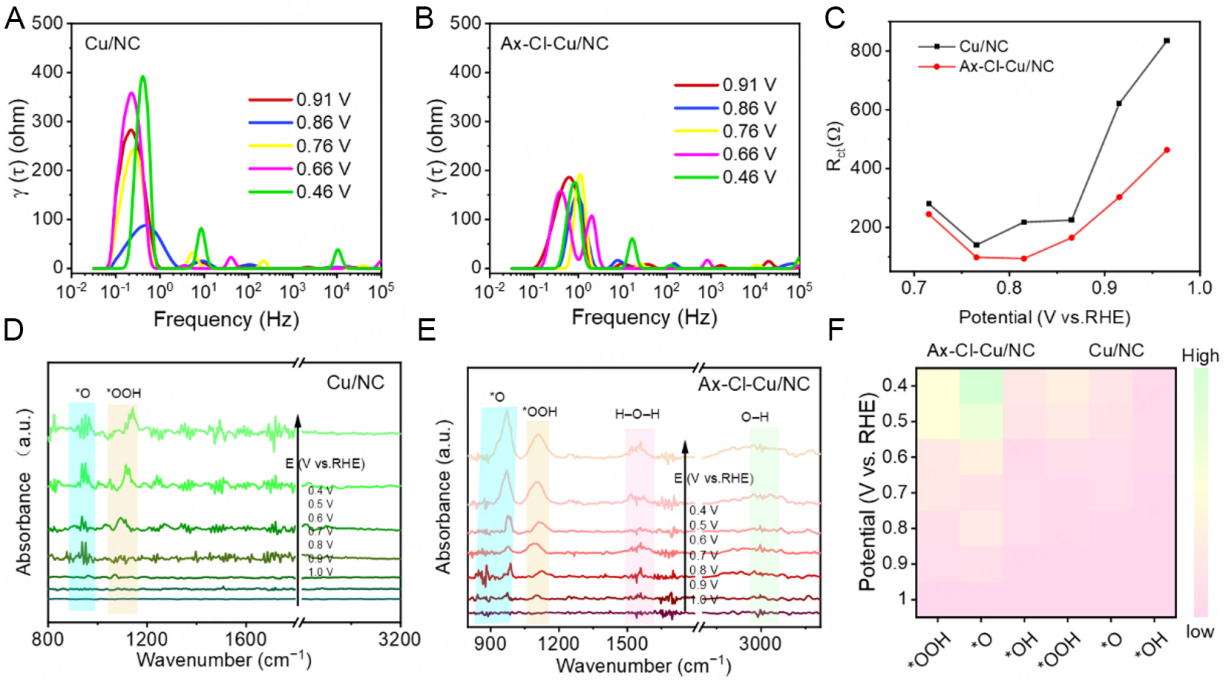

Figure 4. DRT and *in situ* SRIR characterizations. DRT analysis of (A) Cu/NC and (B) Ax-Cl-Cu/NC at different voltages, Charge transfer resistance (RCT) plots of the catalyst under different applied potentials of Ax-Cl-Cu/NC and Cu/NC (C), *in situ* SRIR measurements at different potentials of (D) Cu/NC and (E) Ax-Cl-Cu/NC, (F) Intensity differences of ORR intermediate at Ax-Cl-Cu/NC and Cu/NC.

In-situ SRIR technique monitor the evolution of active species in the ORR process of Ax-Cl-Cu/NC and Cu/NC catalysts, and the regulatory mechanism of coordination Cl on the reaction path was revealed[41]. As shown in Figure 4D and E, both catalysts were tested for potential from 1.0 to 0.4 V in O_2-saturated 0.1 M KOH[42,43]. From the figure, we can see that the infrared spectrum of Cu/NC only shows *O (~900 cm^{-1})[44,45] and *OOH (~1,180 cm^{-1})[46,47] signals, whereas the infrared spectrum of Ax-Cl-Cu/NC also shows H-O-H (~1,630 cm^{-1})[48,49] signals, indicating that the latter more effectively promotes the cleavage of the O-O bond[50-52]. Detailed peak assignments are provided in Supplementary Table 3. The resulting oxygen atoms can quickly combine with proton-electron pairs to form OH, which is further protonated to ultimately produce water (H-O-H). The cleavage of the O-O bond marks the shift of the reaction pathway from a $2e^-$ route to a more efficient $4e^-$ route. The potential-dependent behavior of oxygen intermediates was investigated by SRIR spectroscopy [Figure 4F]. Notably, Ax-Cl-Cu/NC showed much stronger *O signals than Cu/NC, attributed to its enhanced *OOH decomposition capability, facilitating rapid *O formation. *In situ* characterization results not only intuitively confirmed that this catalyst has excellent reaction kinetics. More importantly, by precisely detecting the key reaction intermediates (*O, *OOH) in the ORR, it directly revealed the intrinsic reasons for its high performance, providing experimental evidence for promoting the ORR process.

Zn-air battery performance

In order to verify the practical application value of Ax-Cl-Cu/NC catalyst, it was used as the cathode material to construct ZABs and compared with commercially available Pt/C catalysts[53,54]. The ZAB was assembled using a polished zinc plate as the anode, Ax-Cl-Cu/NC loaded on carbon paper as the air cathode, and 6 M KOH as the electrolyte [Supplementary Figure 19]. All tests were conducted under high-purity O_2 (99.999%) atmosphere at a flow rate of 50 mL min^{-1}, eliminating CO_2 interference and minimizing carbonate formation in the electrolyte. As shown in Figure 5A, the Ax-Cl-Cu/NC equipped ZAB exhibited an OCV of 1.53 V, which was significantly higher than that of the Pt/C based battery of 1.44 V, indicating that the catalyst could

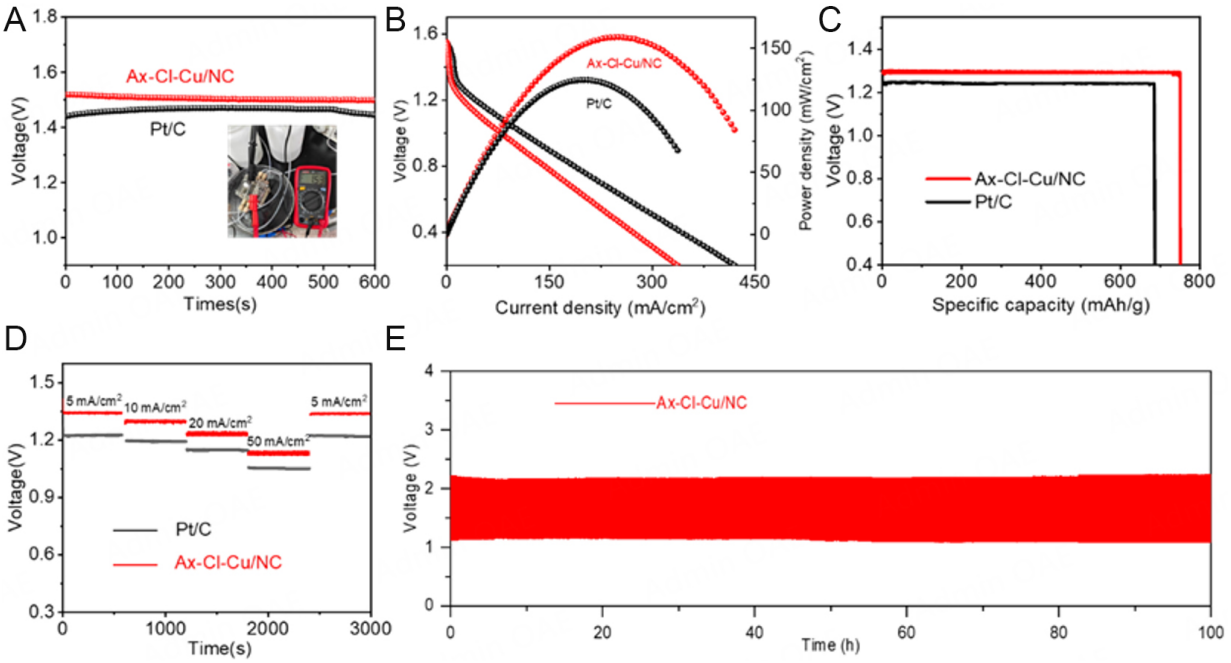

Figure 5. Performance diagram of assembling Zn air battery. (A) Open-circuit voltage plots, (B) Discharge polarization curve and power density plots, (C) specific capacity at current density of 10 mA cm^{-2}, (D) Diagram of galvanostatic discharge curves at different currents of Ax-Cl-Cu/NC and Pt/C, (E) Galvanostatic discharge-charge cycling curve performed under 5 mA cm^{-2} for the Ax-Cl-Cu/NC based ZABs.

drive higher theoretical output voltage of the battery. The discharge polarization curves and power density tests in Figure 5B showed that the Ax-Cl-Cu/NC based ZABs exhibited a maximum output power density of 156.6 mW cm^{-2}, higher than that of the Pt/C based cells at 127.3 mW cm^{-2}, and a superior discharge voltage plateau reflecting a more efficient oxygen reduction kinetics. The performance that surpasses most of the catalysts reported in the literature [Supplementary Table 4]. At a current density of 10 mA cm^{-2}, the specific capacity of the Ax-Cl-Cu/NC based ZAB was 751.1 mA h g_{Zn}^{-1}, which was significantly better than that of the Pt/C based cell (686.4 mA h g_{Zn}^{-1}) [Figure 5C], indicating a more efficient utilization of the zinc anode. The dynamic current density test [Figure 5D] showed that the Ax-Cl-Cu/NC based battery always maintained a higher discharge voltage than the Pt/C based battery when the current density was increased from 5 to 50 mA cm^{-2}. And the discharge potential quickly recovered to the initial level after the current density was reduced to 5 mA cm^{-2}, confirming its excellent multiplicative performance and reversibility. Cycling durability tests showed that the discharge voltage of Ax-Cl-Cu/NC based ZAB did not show any obvious decay after 100 h at a current density of 5 mA cm^{-2}, and the discharge-charge voltage difference remained stable during long-term charging and discharging [Figure 5E], which further verified the long-cycle durability of the catalyst under practical working conditions. However, the Pt/C-based ZAB showed significant performance degradation after 30 h [Supplementary Figure 20]. The above results fully demonstrate that the Ax-Cl-Cu/NC catalyst, with its excellent oxygen reduction performance and stable structural properties, exhibits significant potential for applications in energy storage fields such as zinc air batteries.

CONCLUSION

This study demonstrates that axial chlorine coordination effectively breaks the symmetry constraints of conventional Cu-N_4 catalysts. The resulting Ax-Cl-Cu/NC exhibits remarkable ORR performance due to its optimized electronic structure, achieving a 0.89 V half-wave potential with near-ideal $4e^-$ transfer (n = 3.96) and outstanding stability (< 7 mV decay after 10,000 cycles). Advanced characterization reveals that Cl-induced axial coordination optimizes the interaction between the Cu-N_4 active center and the ORR intermediates, thereby steering the reaction toward a highly favorable $4e^-$ pathway. The work establishes a

novel coordination strategy for designing high-performance SACs while providing fundamental insights into symmetry engineering for electrocatalysis.

DECLARATIONS

Acknowledgments

The authors thank Key Laboratory of Light Energy Conversion Materials of Hunan Province College, for support of the XPS, XAFS, and *in-situ* SRIR technique monitor.

Authors' contributions

Writing-original draft and Data curation: Li, S. (Shuang Li); Li, S. (Shiyu Li)
Formal analysis and Writing-review & editing: Wu, Y.; Wang, J.
Investigation and Formal analysis: Yan, J.; Liu, K.
Methodology and Revised the paper: Su, H.; Yang, Y.

Availability of data and materials

The details of materials and reagents, instrumentation and characterizations, and electrochemical measurements were shown in the Supplementary Materials. Additional data supporting the findings of this study are available from the corresponding author upon reasonable request.

AI and AI-assisted tools statement

Not applicable.

Financial support and sponsorship

This research was funded by the National Natural Science Foundation of China (Grants 12205300, 12575344 to Su, H.), the Hunan Provincial Natural Science Foundation (2024JJ4027 to Su, H.), and the Hunan Normal University Research Program (05311204666 to Su, H.). We are grateful to the 1W1B station at BSRF, BL14W1 and BL20U at SSRF, and BL01B, MCD-A at the National Synchrotron Radiation Laboratory for beamtime access.

Conflicts of interest

Su, H. is Guest Editor of the special issue "Advanced Hydrogen Energy Materials and *in situ* Characterization Technologies" of the journal *Energy Materials*. Su, H. was not involved in any steps of editorial processing, notably including reviewers' selection, manuscript handling and decision making, while the other authors have declared that they have no conflicts of interest.

Ethical approval and consent to participate

Not applicable.

Consent for publication

Not applicable.

Supplementary Materials

Supplementary Materials

REFERENCES

1. Liu, J.; Liu, Y.; Nan, B.; et al. A two-in-one strategy to simultaneously boost the site density and turnover frequency of Fe-N-C oxygen reduction catalysts. *Angew. Chem. Int. Ed.* **2025**, *64*, e202425196. DOI
2. Yang, J.; Liu, W.; Xu, M.; et al. Dynamic behavior of single-atom catalysts in electrocatalysis: identification of Cu-N_3 as an active site for the oxygen reduction reaction. *J. Am. Chem. Soc.* **2021**, *143*, 14530-9. DOI
3. Shang, H.; Zhou, X.; Dong, J.; et al. Engineering unsymmetrically coordinated Cu-S_1N_3 single atom sites with enhanced oxygen reduction activity. *Nat. Commun.* **2020**, *11*, 3049. DOI PubMed PMC

4. Zhang, M.; Li, H.; Chen, J.; et al. Transition metal (Co, Ni, Fe, Cu) single-atom catalysts anchored on 3D nitrogen-doped porous carbon nanosheets as efficient oxygen reduction electrocatalysts for Zn-air battery. *Small* **2022**, *18*, 2202476. DOI
5. Ji, S.; Wang, Y.; Liu, H.; et al. Regulating the electronic synergy of asymmetric atomic Fe sites with adjacent defects for boosting activity and durability toward oxygen reduction. *Adv. Funct. Mater.* **2024**, *34*, 2314621. DOI
6. Wang, Q.; Shang, L.; Sun-Waterhouse, D.; Zhang, T.; Waterhouse, G. Engineering local coordination environments and site densities for high-performance Fe-N-C oxygen reduction reaction electrocatalysis. *SmartMat* **2021**, *2*, 154-75. DOI
7. Bai, J.; Guan, X.; Qu, H.; et al. Multiscale structure regulation induced by fluorine coordination enables high-performance and durable PEMFC. *ACS. Energy. Lett.* **2025**, *10*, 2743-51. DOI
8. Li, J.; Bao, M.; Pan, J.; et al. Chlorine-nitrogen doped hollow polyhedral carbon-based catalysts for high performance zinc-air batteries. *Ind. Eng. Chem. Res.* **2024**, *63*, 19498-505. DOI
9. Shen, H.; Jia, Y.; Qi, Y.; et al. Steering structural mesoporosity and working microenvironment of Fe-N-C catalysts for boosting cathodic mass transport of zinc-air batteries. *Sci. China. Chem.* **2022**, *65*, 1670-8. DOI
10. Tang, C.; Jin, R.; Xia, Y.; et al. Asymmetric low-coordination tailoring of single-atom cobalt catalysts enabling efficient oxygen reduction reaction. *Nano. Energy.* **2025**, *137*, 110776. DOI
11. Wang, P.; Zhang, R.; Wang, K.; et al. Simultaneously constructing asymmetrically coordinated cobalt single atoms and cobalt nanoclusters via a fresh potassium hydroxide clipping strategy toward efficient alkaline oxygen reduction reaction. *Energy. Mater. Adv.* **2023**, *4*, 0042. DOI
12. Kang, Z.; Wang, X.; Wang, D.; et al. Carbon-based single-atom catalysts: impacts of atomic coordination on the oxygen reduction reaction. *Nanoscale* **2023**, *15*, 9605-34. DOI
13. Zhang, L.; Meng, Q.; Zheng, R.; et al. Microenvironment regulation of M-N-C single-atom catalysts towards oxygen reduction reaction. *Nano. Res.* **2023**, *16*, 4468-87. DOI
14. Bai, J.; Lian, Y.; Deng, Y.; et al. Simultaneous integration of Fe clusters and NiFe dual single atoms in nitrogen-doped carbon for oxygen reduction reaction. *Nano. Res.* **2023**, *17*, 2291-7. DOI
15. Wu, M.; Wu, Q.; Yang, Y.; He, Z.; Yang, H. Regulating Lewis acidity and local electron density of iron-based metal organic frameworks via cerium doping for efficient photo-Fenton process. *J. Colloid. Interface. Sci.* **2023**, *630*, 866-77. DOI
16. Ma, N.; Duan, L.; Ma, D.; et al. Demonstration of a high-density alkali-metal atomic magnetometer based on the frequency-symmetrical detuning effect of two pumping lights. *Opt. Express.* **2022**, *30*, 45930. DOI
17. Wang, Q.; Lu, R.; Yang, Y.; et al. Tailoring the microenvironment in Fe-N-C electrocatalysts for optimal oxygen reduction reaction performance. *Sci. Bull.* **2022**, *67*, 1264-73. DOI
18. Xu, Q.; Hu, J.; Yao, H.; et al. Pyridinic-N regulated electron injection to modulate *OH adsorption at Fe-N-C sites for an efficient oxygen reduction reaction. *ACS. Appl. Mater. Interfaces.* **2024**, *16*, 42352-62. DOI
19. Lu, X.; Yang, P.; Wan, Y.; et al. Active site engineering toward atomically dispersed M-N-C catalysts for oxygen reduction reaction. *Coord. Chem. Rev.* **2023**, *495*, 215400. DOI
20. Yu, Z.; Si, C.; Lagrow, A. P.; et al. Iridium-iron diatomic active sites for efficient bifunctional oxygen electrocatalysis. *ACS. Catal.* **2022**, *12*, 9397-409. DOI
21. Gao, H.; Shang, L.; Qian, S.; et al. Precise axial coordination tailors the spin state of single-atom iron for boosted oxygen reduction electrocatalysis. *Adv. Funct. Mater.* **2026**, *36*, e31932. DOI
22. Hu, Y.; Niu, S.; Zhang, Z.; et al. Axial chlorine engineering of p-block antimony atomic sites boosts oxygen reduction. *J. Am. Chem. Soc.* **2025**, *147*, 21231-40. DOI
23. Liu, M.; Liu, Y.; Zhang, X.; et al. Altering the symmetry of Fe-N-C by axial Cl-mediation for high-performance zinc-air batteries. *Angew. Chem. Int. Ed.* **2025**, *64*, e202504923. DOI
24. Yin, L.; Sun, M.; Zhang, S.; Huang, Y.; Huang, B.; Du, Y. Chlorine axial coordination activated lanthanum single atoms for efficient oxygen electroreduction with maximum utilization. *Adv. Mater.* **2024**, *37*, 2416387. DOI
25. Li, L.; Huang, S.; Cao, R.; et al. Optimizing microenvironment of asymmetric N,S-coordinated single-atom Fe via axial fifth coordination toward efficient oxygen electroreduction. *Small* **2021**, *18*, 2105387. DOI
26. Yu, C.; Xiao, W.; Huang, J.; Hao, C.; Shen, P. K.; Tian, Z. Q. Single yttrium atom coordinated by nitrogen and oxygen with an asymmetric 4d orbit as efficient oxygen reduction electrocatalyst. *J. Colloid. Interface. Sci.* **2025**, *691*, 137425. DOI
27. Li, Y.; Zang, K.; Duan, X.; Luo, J.; Chen, D. Boost oxygen reduction reaction performance by tuning the active sites in Fe-N-P-C catalysts. *J. Energy. Chem.* **2021**, *55*, 572-9. DOI
28. Wu, L.; Wang, Y.; Shao, C.; Wang, L.; Li, B. Copper single atom-modulated functionalization of iron clusters on a porous carbon nanosheet for the oxygen reduction reaction. *J. Mater. Chem. A.* **2025**, *13*, 5974-86. DOI
29. Yang, L.; Xu, H.; Liu, H.; et al. Oxygen-reconstituted active species of single-atom Cu catalysts for oxygen reduction reaction. *Research* **2020**, *2020*, 7593023. DOI PubMed PMC

30. Bai, J.; Sun, Z.; Zhang, H.; et al. Modulating the local coordination environment of M-N_x single-atom site for enhanced electrocatalytic oxygen reduction. *Adv. Funct. Mater.* **2024**, *35*, 2417013. DOI
31. Tong, M.; Wang, L.; Fu, H. Designed synthesis and catalytic mechanisms of non-precious metal single-atom catalysts for oxygen reduction reaction. *Small. Methods.* **2021**, *5*, 2100865. DOI
32. Liu, J.; Zhang, W.; Zhang, Y.; et al. Fe, Ni, co-doped ZIF-8 derived in situ grown carbon nanotubes as Zinc-air battery cathode for self-powered electrochemical sensing glucose. *J. Alloys. Compd.* **2025**, *1020*, 179475. DOI
33. Zhang, Y.; Li, F.; Li, S.; et al. Asymmetric dual-atomic catalyst with axial chloride coordination for efficient oxygen reduction reaction. *Adv. Mater.* **2025**, *37*, 2507478. DOI
34. Peng, J.; Hu, B.; Li, Z.; et al. Regulating atomic Fe/Cu dual sites with unsymmetrical Fe-N_6 and Cu-N_1S_2 coordination for promoting bifunctional oxygen electrocatalysis in advanced zinc-air batteries. *Energy. Storage. Mater.* **2024**, *68*, 103342. DOI
35. Cheng, H.; Sun, H.; Dai, M.; et al. Optimizing the ratio of metallic and single-atom Co in CoNC via annealing temperature modulation for enhanced bifunctional oxygen evolution reaction/oxygen reduction reaction activity. *Molecules* **2024**, *29*, 5721. DOI PubMed PMC
36. Wang, M.; Wang, L.; Li, Q.; et al. Regulating the coordination geometry and oxidation state of single-atom Fe sites for enhanced oxygen reduction electrocatalysis. *Small* **2023**, *19*, 2300373. DOI
37. Xie, S.; Jin, H.; Wang, C.; et al. A comparison study on single metal atoms (Fe, Co, Ni) within nitrogen-doped graphene for oxygen electrocatalysis and rechargeable Zn-air batteries. *Chin. Chem. Lett.* **2023**, *34*, 107681. DOI
38. Sabhapathy, P.; Raghunath, P.; Sabbah, A.; et al. Axial chlorine induced electron delocalization in atomically dispersed FeN_4 electrocatalyst for oxygen reduction reaction with improved hydrogen peroxide tolerance. *Small* **2023**, *19*, 2303598. DOI
39. Chen, Y.; Liu, X.; Li, S.; Li, J.; Fan, M.; Shu, S. Crystalline-amorphous heterostructures with built-in electric fields enhance the tandem electroreduction of nitrate to ammonia. *Adv. Funct. Mater.* **2025**, *36*, e21409. DOI
40. Li, S.; Huang, J.; Yan, J.; et al. Electronic bridges-stabilized Fe-Cu twin-sites circumvent scaling relationship for robust acidic oxygen reduction. *ACS. Catal.* **2026**, *16*, 2124-34. DOI
41. Jia, B.; Xie, X.; Lin, J.; et al. Harnessing pyridinic N vacancy defect in microporous structures to induce the pre-adsorption of oxygen and boost oxygen reduction reaction kinetics. *Angew. Chem. Int. Ed.* **2025**, *64*, e202508674. DOI
42. Chen, X.; Hu, H.; Liu, M.; Zhong, X.; Wu, D.; Su, H. Unveiling the spatially dependent cooperative effect in iridium sites for enhanced acidic water oxidation. *Nano. Lett.* **2025**, *25*, 15384-92. DOI
43. Liu, M.; Su, H.; Liu, X.; et al. Dynamic modulation of electron redistribution at the heterogeneous interface nickel hydroxides/platinum boosts acidic oxygen reduction reaction. *Nat. Commun.* **2025**, *16*, 2826. DOI PubMed PMC
44. Wang, M. J.; Ji, R.; Huang, C.; et al. Synergistic strong-weak adsorption coupling in the FeN_6-CoN_4 dual-site modulates oxygen reduction pathways via oxygen adsorbate evolution-to-dissociation transition. *ACS. Catal.* **2026**, *16*, 2800-13. DOI
45. Xu, S.; Zhang, Y.; Peng, Y.; et al. Breaking the scaling relationship for oxygen reduction*via* amino-molecule-interface-mediated metallene electrocatalysts. *Chem. Sci.* **2026**, *17*, 7590-8. DOI PubMed PMC
46. Liu, C.; Cheng, K.; Chen, Q.; et al. Synergy of nickel single-atom and heteroatoms Co-doping in carbon for efficient hydrogen peroxide electrosynthesis. *Angew. Chem. Int. Ed.* **2025**, *65*, e21397. DOI
47. Liu, J.; Zhang, Z.; Han, C.; et al. Ligand-modified nickel nitride for natural seawater H_2O_2 synthesis. *Appl. Catal. B. Environ. Energy.* **2025**, *373*, 125362. DOI
48. Liu, Z.; Mo, M.; Xiao, B.; et al. Asymmetric coordination modulation on Co single-atom sites tunes selectivity of acidic oxygen reduction. *Appl. Catal. B. Environ. Energy.* **2025**, *377*, 125510. DOI
49. Xia, H.; Sun, M.; Yang, D.; et al. Phosphorus/Sulfur-modulated p-band center of pentagonal carbon for efficient oxygen reduction reaction. *J. Am. Chem. Soc.* **2025**, *147*, 41472-80. DOI
50. Xia, P.; He, T.; Sun, Y.; et al. Defective-engineered ZnO encapsulated in N-doped carbon for sustainable $2e^-$ ORR: interfacial Zn-N bond regulated oxygen reduction pathways. *ACS. Catal.* **2024**, *14*, 12917-27. DOI
51. Wang, Y.; Zheng, M.; Li, Y.; et al. p-d orbital hybridization induced by a monodispersed Ga site on a Pt_3Mn nanocatalyst boosts ethanol electrooxidation. *Angew. Chem. Int. Ed.* **2022**, *61*, e202115735. DOI
52. Wang, J.; Liu, W.; Luo, G.; et al. Synergistic effect of well-defined dual sites boosting the oxygen reduction reaction. *Energy. Environ. Sci.* **2018**, *11*, 3375-9. DOI
53. Liao, Y.; Xiao, Y.; Li, Z.; et al. Structural engineering of Co-metal-organic frameworks via Ce incorporation for improved oxygen evolution. *Small* **2023**, *20*, 2307685. DOI
54. Song, L.; Liu, Y.; Wang, J.; et al. Hierarchically porous two-dimensional Fe/N-codoped carbon nanoleaves for enhanced mass transfer and electrocatalytic oxygen reduction reaction. *Energy. Mater.* **2025**, *5*, 500139. DOI